

SAR TOMOGRAPHY AS AN ADD-ON TO PSI: GAIN IN DEFORMATION SAMPLING VIS-A-VIS QUALITY OF THE DETECTED SCATTERERS

Muhammad A. Siddique¹, Urs Wegmüller², Irena Hajnsek^{1,3}, Othmar Frey^{1,2}

¹Earth Observation and Remote Sensing, ETH Zurich, Switzerland

²Gamma Remote Sensing AG, Gümligen, Switzerland

³Microwaves and Radar Institute, German Aerospace Center - DLR, Oberpfaffenhofen, Germany

ABSTRACT

SAR tomography can be used as an add-on to persistent scatterer interferometry (PSI) to increase deformation sampling in urban areas by resolving the frequently occurring layovers that are by definition rejected in the PSI processing. This paper, while focusing on the case of a typical high-rise building in layover, quantitatively assesses the potential gain in deformation sampling achieved by the added use of an advanced SAR tomographic technique relative to a PSI approach. At the same time, the quantity of the detected scatterers is weighed against their quality, as assessed on the basis of root-mean-square (RMS) phase deviation between the measurements and the model fit. The quality of the scatterers is also compared with the quality of the persistent scatterers as identified with a PSI approach. The experiments are performed on an interferometric stack of 50 TerraSAR-X stripmap mode images.

Index Terms— SAR tomography, persistent scatterer interferometry, multi-baseline interferometry, TerraSAR-X

1. INTRODUCTION

Persistent scatterer interferometry (PSI) [1, 2] is nowadays operationally used for spaceborne SAR-based deformation assessment. A *persistent* scatterer (PS) is by definition a single dominant scatterer exhibiting point-like behavior. Therefore, PSI typically rejects layovers where multiple point scatterers of comparable energy are superposed in the same resolution cell, which in turn limits deformation retrieval in areas where layovers are prevalent. SAR tomography [3, 4, 5] is a means to resolve layovers which motivates its use as an add-on to PSI. Advanced SAR tomographic techniques [6, 7, 8, 9] allow simultaneous estimation of the elevation and deformation parameters for the multiple scatterers overlaid in the same pixel, and thereby promise an improvement in deformation sampling. From the perspective of an operational

combination of SAR tomography and PSI [10, 11, 8], it is important to quantitatively assess how significant is the gain in deformation sampling with the added use of tomography, and whether the quality of the scatterers obtained with tomography is comparable with the quality of the persistent scatterers as identified with an established PSI approach. This paper addresses the aforementioned concerns, while focusing on the case of a typical high-rise building suffering from layover.

The methodology adopted in this paper is as follows. First, we obtain a PSI solution for the observed area using the Interferometric Point Target Analysis (IPTA) [2] framework, which comprises iteratively computed residual topography, deformation parameters (linear deformation velocity and phase-to-temperature sensitivity [11, 12]) and atmospheric phase screen (APS) for each PS. Next, we perform a tomographic analysis on the entire area (including the pixels which were not identified as PSs in the IPTA-based PSI processing). The unknown scatterer elevation (distance along the perpendicular to line of sight direction) and deformation parameters are estimated with the maximization of a beamforming-based reflectivity function [8, 11]. A generalized likelihood ratio (GLRT) [4] test is used to detect single and double scatterers. The quality of the scatterers is evaluated in terms of the root-mean-square (RMS) phase deviation between the measurements and the model fit, and compared against the quality of the PSs. The gain in deformation sampling (relative to the number of the PSs identified in the observed area) is quantitatively assessed vis-a-vis the corresponding quality of the scatterers over a range of detection thresholds.

2. SINGLE-LOOK TOMOGRAPHIC PROCESSING

Considering the single-look complex (SLC) measurement vector, \mathbf{y} represents a maximum of two temporally coherent point scatterers in a given range-azimuth pixel, we make the following hypotheses [4, 11]:

$$\mathcal{H}^0 : \mathbf{y} = \mathbf{n} \quad (1)$$

$$\mathcal{H}^1 : \mathbf{y} = \gamma_1 \mathbf{a}(\mathbf{p}_1) + \mathbf{n} \quad (2)$$

$$\mathcal{H}^2 : \mathbf{y} = \gamma_1 \mathbf{a}(\mathbf{p}_1) + \gamma_2 \mathbf{a}(\mathbf{p}_2) + \mathbf{n}. \quad (3)$$

This research project has been funded by the Swiss Space Office, State Secretariat for Education and Research of the Swiss Confederation (SER/SSO), via the MdP2012 initiative.

γ is the target reflectivity. $\mathbf{a}(\mathbf{p})$ is the steering vector as a function of the parameter vector, $\mathbf{p} = [s, \nu, \kappa]$, comprising the unknown elevation, s linear deformation velocity, ν and phase-to-temperature sensitivity, κ of the scatterer(s). The subscripts 1 and 2 mark the first and the second scatterer, respectively, with the energy of the first being more than (or equal to) the energy of the second scatterer. \mathbf{n} represents the additive noise. The structure of the steering vector, for N baselines, is given by:

$$\mathbf{a}(\mathbf{p}) = [1 \quad e^{-j\varphi_1(\mathbf{p})} \quad \dots \quad e^{-j\varphi_{N-1}(\mathbf{p})}]^T. \quad (4)$$

where φ_n is the interferometric phase modeled as follows:

$$\varphi_n(\mathbf{p}) = 2k \left[\Delta r_n(s) + \nu t_n + \frac{1}{2k} \kappa \tau_n \right] \quad (5)$$

for $n = 0, 1, \dots, N-1$. $\Delta r_n(s)$ is the sensor-to-target path-length difference, t_n is the temporal baseline, and τ_n is the temperature change (with respect to the temperature for the reference layer, $n = 0$), for the n^{th} interferometric layer.

$$\Delta r_n(s) = r_n(s) - r_0(s) \approx \frac{s^2}{2(r_0 - b_n^{\parallel})} - \frac{b_n^{\perp} s}{r_0 - b_n^{\parallel}} \quad (6)$$

where b_n^{\perp} and b_n^{\parallel} are the orthogonal and parallel components of the n^{th} spatial baseline, respectively. The phase model in eq. 5 assumes that the deformation of the scatterer(s) is composed of two forms of motion in the line of sight (LOS) – a temporally linear displacement and a temperature-dependent dilation due to the thermal expansion of the building structures [12, 11].

The parameter vectors for a potential first and second scatterer, \mathbf{p}_1 and \mathbf{p}_2 , respectively, are estimated as follows [4, 11]:

$$\hat{\mathbf{p}}_1 = \arg \max_{\mathbf{p}} (|\mathbf{a}^H(\mathbf{p}) \mathbf{y}|). \quad (7)$$

$$\hat{\mathbf{p}}_2 = \arg \max_{\mathbf{p}} \left(\frac{|\mathbf{a}^H \mathbf{y}_c|^2}{\|\mathbf{y}_c\|^2} \right), \quad (8)$$

where $\mathbf{y}_c = \hat{\mathbf{P}}_1^{\perp} \mathbf{y}$ and $\hat{\mathbf{P}}_1^{\perp} = \mathbf{I}_N - \frac{\mathbf{a}(\hat{\mathbf{p}}_1) \mathbf{a}^H(\hat{\mathbf{p}}_1)}{N}$.

2.1. Scatterer detection

The *sequential generalized likelihood ratio test with cancellation* (SGLRTC), as proposed in [4], is used to test the three hypotheses: \mathcal{H}_0 , \mathcal{H}_1 , and \mathcal{H}_2 , viz. noise only, single scatterer, and double scatterer, respectively. SGLRTC is a sequential two-step test; first, it decides whether the pixel is a double scatterer or not, i.e.,

$$\left(\frac{|\mathbf{u}_c^H \mathbf{y}_c|^2}{\|\mathbf{y}_c\|^2} \right) \underset{\mathcal{H}_2}{\overset{\mathcal{H}_1}{\gtrless}} T_2 \quad (9)$$



Fig. 1. TerraSAR-X average backscatter image of Diagonal Mar, Barcelona, Spain. An example layover-affected building is highlighted in red.

where $\mathbf{u}_c = \hat{\mathbf{P}}_1^{\perp} \mathbf{a}(\hat{\mathbf{p}}_2) / \|\hat{\mathbf{P}}_1^{\perp} \mathbf{a}(\hat{\mathbf{p}}_2)\|$ and $\mathbf{y}_c = \hat{\mathbf{P}}_1^{\perp} \mathbf{y}$. If the hypothesis \mathcal{H}_2 is rejected, a second test is made between \mathcal{H}^0 and \mathcal{H}^1 as follows:

$$\left(\frac{|\mathbf{a}^H(\hat{\mathbf{p}}_1) \mathbf{y}|^2}{N^2 \|\mathbf{y}\|^2} \right) \underset{\mathcal{H}^0}{\overset{\mathcal{H}^1}{\gtrless}} T_1. \quad (10)$$

The detection thresholds, T_1 and T_2 , are set at the same value to jointly maximize the probabilities of detection for both the single and double scatterers for a given probability of false alarm (as suggested in [4]).

2.2. Quality of the detected scatterers

The estimated SLC vector, \mathbf{y}_{est} (model fit) is computed as follows:

$$\mathbf{y}_{est} = \begin{cases} \hat{\gamma}_1 \mathbf{a}(\hat{\mathbf{p}}_1) & \text{single scatterer} \\ \hat{\gamma}_1 \mathbf{a}(\hat{\mathbf{p}}_1) + \hat{\gamma}_2 \mathbf{a}(\hat{\mathbf{p}}_2) & \text{double scatterer} \end{cases} \quad (11)$$

where $\hat{\gamma}_1$ and $\hat{\gamma}_2$ are the estimated reflectivities of the first and second scatterer, respectively: $\hat{\gamma}_1 = \mathbf{a}^H(\hat{\mathbf{p}}_1) \mathbf{y}$ and $\hat{\gamma}_2 = \mathbf{a}^H(\hat{\mathbf{p}}_2) \mathbf{y}_c / \|\hat{\mathbf{P}}_1^{\perp} \mathbf{a}(\hat{\mathbf{p}}_2)\|$. The quality of the parameter estimation for the detected scatterers is assessed in terms of goodness of fit as represented by the root-mean-square (RMS) phase deviation, σ_r^{tomo} between the SLC measurements and the tomographic model fit (which is consistent with the quality assessment in the IPTA processing):

$$\sigma_r^{tomo} = \sqrt{\frac{1}{N-1} \sum_{n=1}^N (\varphi_n^{res})^2} \quad (12)$$

where φ_n^{res} is the angle difference between \mathbf{y} and \mathbf{y}_{est} for the n^{th} interferometric layer. The lower the σ_r^{tomo} , the better is the perceived quality of the scatterer.

2.3. Relative gain in deformation sampling

The gain in deformation sampling, G offered by SAR tomographic processing relative to a PSI-based analysis of a given

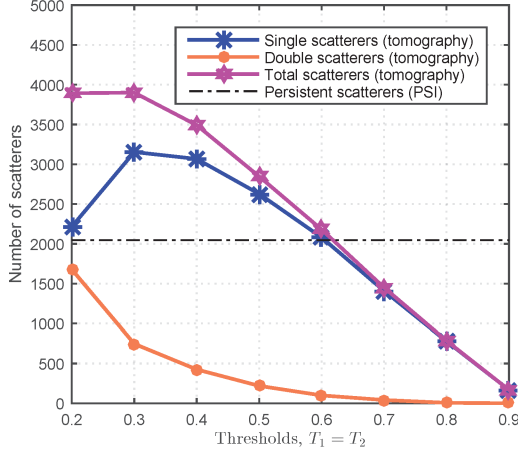


Fig. 2. Number of point-like scatterers obtained with tomographic inversion versus the thresholds of detection, T_1 and T_2 , keeping $T_1 = T_2$, for the building highlighted in red in Fig. 1. The number of persistent scatterers identified with the IPTA-based PSI processing, is also shown for reference.

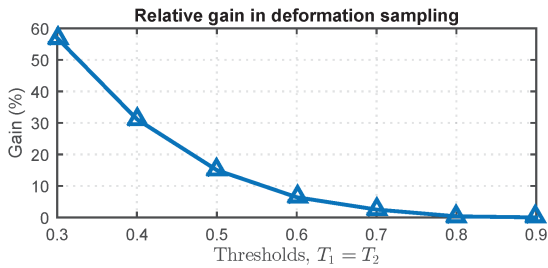


Fig. 3. The relative gain in the deformation sampling (achieved with tomography processing in addition to the IPTA-based PSI analysis) at different thresholds of detection.

area is defined as follows:

$$G = \left(\frac{2N_{d,u} + N_{d,ps}}{N_{psi}} \right) \times 100\% \quad (13)$$

where $N_{d,ps}$ is the number of those pixels that are detected as double scatterers but were also identified as PSs, $N_{d,u}$ is the number of pixels that are uniquely detected as double scatterers, i.e. the pixels were not identified as PSs, and N_{psi} is the total number of PSs identified in the PSI processing.

3. RESULTS

The experiment has been performed on an interferometric data stack of 50 TerraSAR-X stripmap scenes acquired over the city of Barcelona between 2007-2012. The results reported in this paper are for a high-rise building in layover, as highlighted in Fig. 1. A PSI solution was obtained using the Interferometric Point Target Analysis (IPTA) [2] framework. The data was phase calibrated and a tomographic analysis was conducted in succession. The number of scatterers obtained with tomography are shown in Fig. 2 for a range of

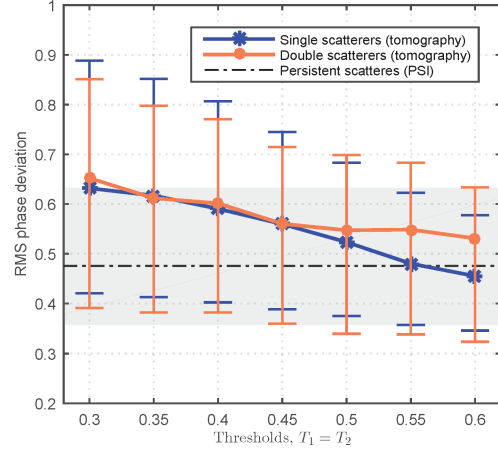


Fig. 4. The variation in RMS phase deviation for single and double scatterers obtained with tomography against different thresholds of detection. The vertical bars represent the interquartile range around the median values. The shaded gray region encloses the interquartile range, and the dashed black line shows the median value of the RMS phase deviation, for the persistent scatterers identified with IPTA-based PSI processing.

detection thresholds, and the corresponding gain in deformation sampling relative to the IPTA-based PSI analysis is as shown in Fig. 3. The quality of the scatterers, as evaluated in terms of RMS phase deviation, σ_r^{tomo} is shown in Fig. 4. These results show, as a general trend, that with increasing thresholds, the quantity of the detected scatterers decreases while the quality tends to improve. The scatterers detected at $T_1 = T_2 = 0.4$ are projected to Google Earth 3D building model, as shown in Fig. 5.

4. DISCUSSION

An increase in the values of the detection thresholds, T_1 and T_2 , makes the decision criteria in eqs. 9 and 10 more stringent, and therefore, leads to a decrease in the number of the detected scatterers. However, for thresholds below 0.3, we observe an irregularity in the trend due to a jump in the number of double scatterers accompanied by a sharp decline in the number of double scatterers with decreasing thresholds. This behavior can be explained in terms of the SGLRTC decision strategy. It first tests the hypothesis that a given pixel is a double scatterer: if the threshold T_2 is too low, many pixels can get falsely classified as double scatterers before being explicitly tested for single scatterers. For thresholds higher than 0.6, the total number of detected scatterers falls below the number of persistent scatterers (PSs) identified with the IPTA-based PSI processing, and as shown in Fig. 3, the relative gain in deformation sampling with layover separations, G drops to very low values. It is, therefore, appropriate in our case to choose thresholds between 0.3–0.6. The quality

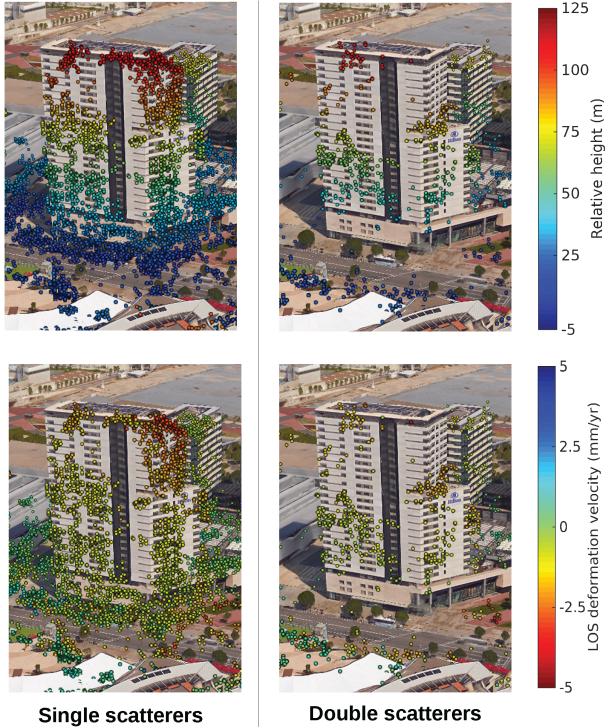


Fig. 5. Single and double scatterers obtained with tomographic analysis. The thresholds of detection, $T_1 = T_2 = 0.4$. The colors represent estimated parameters. Top row: Relative height. Bottom row: LOS Average deformation velocity.

of the detected single and double scatterers, as evaluated in terms of RMS phase deviation, σ_r^{tomo} is as shown in Fig. 4. It be seen that the quality improves with increasing thresholds. We also compare the quality of the detected scatterers against the quality of PSs. For thresholds at 0.55 and above, the quality of the single scatterers becomes comparable to or better than the quality of the PSs. However, the quality of the double scatterers remains generally lower than the quality of the PSs. For thresholds above 0.6, we have too few double scatterers to capture the statistics. These findings imply, in order that the quality of the single scatterers is comparable with the quality of the PSs, the requisite detection thresholds may become too prohibitive to allow for a sufficient gain in deformation sampling. Nonetheless, with a slight compromise, we can achieve as much as 30% relative gain in deformation sampling (for $T_1 = T_2 = 0.4$), while the median values of σ_r^{tomo} for the single and double scatterers are at 0.6 rad or below.

5. CONCLUSION

This paper has investigated the utility of SAR tomography as an add-on to PSI for deformation analysis in the case of a layover-affected high-rise building. The gain in deformation sampling that can be achieved by the added use of a beamforming-based single-look tomographic processing, rel-

ative to a PSI analysis with the IPTA framework, has been quantitatively and qualitatively assessed. The results show that there is a trade-off between the quantity and the quality of the scatterers obtained with tomography. In order that the quality of the detected single scatterers is comparable with the quality of the persistent scatterers identified in the PSI processing, the requisite thresholds may be too high to allow for the detection of a sufficient number of double scatterers. However, with a slight compromise, SAR tomography allows for a significant improvement in deformation sampling.

6. REFERENCES

- [1] A. Ferretti, C. Prati, and F. Rocca, "Permanent scatterers in SAR interferometry," *IEEE Trans. on Geosc. and Remote Sens.*, vol. 39, no. 1, pp. 8–20, 2001.
- [2] C. Werner, U. Wegmüller, T. Strozzi, and A. Wiesmann, "Interferometric point target analysis for deformation mapping," in *Proc. IEEE Int. Geosci. Remote Sens. Symp.*, 2003, pp. 4362–4364.
- [3] O. Frey and E. Meier, "3-D time-domain SAR imaging of a forest using airborne multibaseline data at L- and P-bands," *IEEE Trans. on Geosc. and Remote Sens.*, vol. 49, no. 10, pp. 3660–3664, 2011.
- [4] A. Pauciuolo, D. Reale, A. De Maio, and G. Fornaro, "Detection of double scatterers in SAR tomography," *IEEE Trans. Geosci. Remote Sens.*, vol. 50, no. 9, pp. 3567–3586, 2012.
- [5] A. Reigber and A. Moreira, "First demonstration of airborne SAR tomography using multibaseline L-Band data," *IEEE Trans. Geosci. Remote Sens.*, vol. 38, no. 5, pp. 2142–2152, 2000.
- [6] F. Lombardini, "Differential tomography: A new framework for SAR interferometry," *IEEE Trans. Geosci. Remote Sens.*, vol. 43, no. 1, pp. 37–44, 2005.
- [7] X. Zhu and R. Bamler, "Superresolving SAR tomography for multidimensional imaging of urban areas: Compressive sensing-based TomoSAR inversion," *IEEE Signal Process. Mag.*, vol. 31, no. 4, pp. 51–58, 2014.
- [8] M. Siddique, I. Hajnsek, U. Wegmüller, and O. Frey, "Investigating the combined use of differential SAR tomography and PSI for spatio-temporal inversion," in *Proc. Joint Urban Remote Sens. Event*, 2015.
- [9] D. Reale, G. Fornaro, and A. Pauciuolo, "Extension of 4-D SAR imaging to the monitoring of thermally dilating scatterers," *IEEE Trans. Geosci. Remote Sens.*, vol. 51, no. 12, pp. 5296–5306, 2013.
- [10] O. Frey, M. Siddique, I. Hajnsek, U. Wegmüller, and C. Werner, "Combining SAR tomography and a PSI approach for high-resolution 3-D imaging of an urban area," in *Proc. 10th European Conf. on SAR*, 2014, pp. 1045–1048.
- [11] M. Siddique, U. Wegmüller, I. Hajnsek, and O. Frey, "SAR tomography for spatio-temporal inversion of point-like scatterers in urban areas," in *Proc. IEEE Int. Geosci. Remote Sens. Symp.*, July 2015, pp. 5272–5275.
- [12] U. Wegmüller and C. Werner, "Mitigation of thermal expansion phase in persistent scatterer interferometry in an urban environment," in *Proc. Joint Urban Remote Sens. Event*, March 2015, pp. 1–4.